Separation and Purification Technology 149 (2015) 470–478

Contents lists available at ScienceDirect

Separation and Purification Technology

journal homepage: www.elsevier.com/locate/seppur

Fabrication of highly porous glass filters using capillary suspension processing

Johannes Maurath [a,*], Jens Dittmann [a], Niko Schultz [b], Norbert Willenbacher [a]

[a] Karlsruhe Institute of Technology, Institute for Mechanical Process Engineering and Mechanics, Gotthard-Franz-Strasse 3, 76131 Karlsruhe, Germany
[b] SCHOTT AG, Corporate R&D, Hattenbergstrasse 10, 55122 Mainz, Germany

ARTICLE INFO

Article history:
Received 8 April 2015
Received in revised form 17 June 2015
Accepted 18 June 2015
Available online 19 June 2015

Keywords:
Porous glass filters
Capillary suspension processing
Pore structure
Mechanical strength
Permeability coefficient

ABSTRACT

We present a novel, capillary suspension based processing route for sintered glass filters with porosities $\geqslant$50% at average pore sizes between 1 and 50 μm. This new kind of glass filters exhibits narrow pore size distribution and uniform pore structure. Pores are exceptionally smooth and round. Accordingly, permeability and mechanical strength of these filters excel that of similarly processed ceramic and commercial glass filters significantly.

Mechanical strength at a given porosity is much higher than that of commercial glass filters and reaches values similar to that of ceramic filters with distinctly higher matrix strength. Absolute values are well predicted by the Gibson & Ashby model $\sigma_c/\sigma_{f,0} = B_0(1-\varepsilon)^z$ with $B_0 = 0.8$. Liquid permeability varies with pore size according to Darcy's law but absolute values are clearly higher than that for ceramic filters at given pore size as expected from the smoother pore structure. Gas permeability is especially high at pore sizes <10 μm and exceeds that of ceramic and commercial glass filters significantly. Moreover, this results in a weaker than quadratic pore size dependence. This is presumably due to slip effects occurring especially in small pores and narrow necks of the novel glass filters.

© 2015 Elsevier B.V. All rights reserved.

1. Introduction

In the field of microfiltration the increasing number of applications at high temperatures, covering greater pH ranges and including chemically more aggressive media results in a need of inorganic filter media [1,2]. Inorganic filters become increasingly popular for large volume solid–liquid separation processes such as in waste water recycling or drinking water treatment [3,4]. Furthermore, inorganic filters or membranes find their applications in industrial hot gas cleaning processes [5] or for the purification of liquid metals [6]. As polymeric materials cannot withstand the extreme conditions regarding temperature, chemical and mechanical resistance occurring in the exemplified applications, there is a strong trend to ceramic and glass filter media for industrial purposes. Their outstanding chemical resistance is a key advantage of glass filters. Since the chemical resistance is dependent of the composition of the glass itself, it is obvious to choose an appropriate glass for the respective scope of application. Borosilicate glasses are examples for high resistant glasses which are applied for nearly all kinds of laboratory glassware. Their hydrolytic, acidic and basic resistance is high even at elevated temperatures. Furthermore, these properties are for some kinds of glasses combined with a high thermal shock resistance. Therefore, potential fields of application of the glass filters presented here range from beverage industries [3,7], over gas filtration purposes to applications in laboratory equipment. The smooth pore structure and the narrow pore size distribution are promising indicators for a good fouling resistance, good back flushing behavior and a narrow cut-off range. As the manufacturing of fine granulated and fractured glass powders can be expensive, but the sintering process is performed at temperatures well below sintering temperatures of ceramic materials, the specific costs of these glass filters range in between polymer and ceramic filters.

Typical established filters made of glass are either fiber filters, leached glass membranes, porous silica glass prepared via the sol–gel process or sintered glasses. Nearly all subsequently summarized manufacturing methods not only apply to glass but also for manufacturing metallic [8,9] or ceramic filters [10,11], while sol–gel processes are exclusively for non-metallic materials and leaching is a typical manufacturing method for microporous glass membranes. For fiber filters in pad or blanket form the thin glass fibers are bound together by their intrinsic properties or by impregnation of the sheets with suitable resins or adhesives. Typical pore sizes are in the range of 1 up to 50 μm [12,13]. Via phase separation and leaching of alkali glasses porous membranes

* Corresponding author.
E-mail address: johannes.maurath@kit.edu (J. Maurath).

http://dx.doi.org/10.1016/j.seppur.2015.06.022
1383-5866/© 2015 Elsevier B.V. All rights reserved.

with pore sizes in the range of 1–1000 nm are achieved. After forming the glass part a heat treatment in the temperature range between 500 and 700 °C initiates a phase separation. Two different phases arise from the homogeneous glass, while an alkali-rich phase can be leached out by mineral acids, alcohols or water at moderate temperature (RT up to 100 °C). Since the other phase is almost pure silica, a porous glass with silica content of about 96% is achieved [14]. Glasses with pore sizes below 1 μm also result from the sol gel-process. Here a silicate suspension gets gelled in a chemical reaction, dried and sintered in a following heat treatment [15]. The processes introduced above are most common but porous glass filters can also be produced via sintering processes. This provides better control of pore size, porosity, pore shape and uniformity. Sintered filters own a higher mechanical strength and a higher heat resistance than the cheaper glass fiber filters, where organic binders often limit the operating temperature [16]. The sintering of glass powder via the sacrificial templating method where additional fillers (e.g. salts, organic materials) are added as pore forming agents is limited to pore sizes between 20 and 200 μm [14]. A further technique for manufacturing porous sintering materials is the replica technique. Natural or synthetic organic templates are filled with a suspension of glass particles. After drying of the infiltrated templates all organic components get pyrolized in a debinding step, the following sintering step consolidates the replicated structure [14,17], and typically pore sizes >10 μm are achieved [10]. Enke et al. [14,17] reported about the combination of these two methods with the leaching technique. Glass monoliths with a hierarchical porosity and a bimodal pore size distribution can be manufactured. Furthermore, the partial sintering is a common manufacturing method for porous sintering materials. The final products exhibit a wide size range of open pores [10,18]. Various companies (e.g. DURAN Group GmbH, Heraeus Quarzglas GmbH & Co. KG) produce porous glass frits and filters in the pore size range between 1 and 300 μm, while in products with pore sizes <60 μm porosities are well below 40%.

The processing route based on capillary suspensions as presented here allows for manufacturing sintered filters with a porosity >50% and average pore sizes in a range of 1–50 μm. Porosity and pore sizes are the result of the controlled heterogenization of suspensions using capillary forces. The particle network structure of these so-called capillary suspensions can be preserved even in the sintered part. Ceramic capillary suspensions were already successfully applied as precursors for manufacturing porous ceramics [19,20].

Capillary suspensions, disperse systems consisting of a solid and two immiscible fluid phases, represent a distinct class of materials. Particles are essentially suspended in the major or so-called bulk fluid phase. The secondary fluid phase occupies only a small fraction of the liquid volume (<5 vol%), which is trapped in the capillary bridges formed at the particle contact points [21].

Adding an appropriate secondary liquid phase to a suspension changes the rheological behavior from fluid or weakly elastic to gel-like. In the pure suspension the particles are either well dispersed or they form already a sample-spanning fractal network due to dominating van-der-Waals attraction. Upon addition of the secondary fluid capillary bridges between particles are formed.

Since capillary suspensions based on glass and ceramic particles show such a strong and easy to control structure formation they can be used as precursor for highly porous sintering materials. The homogeneous sample spanning network can be preserved even during debinding and completely open-porous sintered parts are accessible. The manufacturing of macroporous ceramic sintered parts based on capillary suspensions [19] and their microstructure and mechanical strength in dependence of secondary phase content [20] have been described earlier. Now we discuss the processing of sintered glass filters manufactured with this new processing route. We demonstrate that the filters based on capillary suspensions and glass powder show significant advantages regarding permeability compared to ceramic and commercial glass filters. Moreover, the mechanical strength reaches similar values as ceramic filters at a given porosity.

2. Experimental

The experiments were carried out using a capillary suspension system based on glass with a composition similar to borosilicate glass in three different particle sizes as solid phase, paraffin oil as bulk fluid phase and an aqueous sucrose solution as the secondary fluid phase. With this material system we fabricated sintered parts for microstructural characterization, mechanical strength measurements and filtration tests.

2.1. Raw materials

Glass powders with compositions similar to borosilicate glasses (Technical Glass G018-361; SCHOTT AG, Mainz, Germany) with three different particle sizes and density $\rho = 2.75$ g/cm^3 were used. The particle size distribution as determined through Fraunhofer diffraction (Helos H0309; Sympatec GmbH, Clausthal-Zellerfeld, Germany) using in water dispersed particles in an ultrasonic wet dispersing unit (Quixel and Cuvette, Sympatec GmbH) for all three glass species is shown in Fig. 1. Obviously, Glass 2 exhibits a monomodal fairly narrow particle size distribution, whereas the other two powders show a broad slightly bimodal size distribution. The average volume based diameters are $x_{50,3} = 11.0$ μm (glass 1), $x_{50,3} = 1.1$ μm (glass 2) and $x_{50,3} = 0.6$ μm (glass 3). Scanning-electron-microscopy (SEM) micrographs (S-4500; Hitachi High-Technologies Europe GmbH, Krefeld, Germany) helped to get information about the particle morphology (Fig. 1). The bulk phase was paraffin oil (Carl Roth, Karlsruhe, Germany) with a Newtonian flow behavior and a dynamic viscosity $\eta(20\ °C) = 0.03$ Pa s. To prevent unwanted agglomeration in the pure suspensions of glass 3 the nonionic wetting agent Polysorbat 20 (Tween20; Carl Roth, Karlsruhe, Germany) with HLB = 16.7 was used. The secondary phase was a 1.853 M aqueous sucrose solution. The D(+)-sucrose (Carl Roth, Karlsruhe, Germany) was dissolved in distilled water at 20 °C. The solution shows a dynamic viscosity of $\eta(20\ °C) = 0.08$ Pa s.

2.2. Processing route

The main processing steps for manufacturing porous glasses based on capillary suspensions are summarized in the following flow sheet (Fig. 2). Pure suspensions were prepared by mixing the solid powder into the bulk phase with a high shear dissolver at a speed of 1200 rpm for 10 min. For a better homogenization the pure suspensions were then treated in a self-constructed ball mill for 24 h. Adding a small amount of surfactant (0.7 vol% of the bulk fluid phase) to suspensions consisting of glass 3 prevents unwanted agglomeration. The capillary network formation is induced by adding the secondary fluid phase to the pure suspension again using a high shear dissolver at a speed of 800 rpm for 5 min, followed by a period of 2 min with reduced stirring speed at 500 rpm. A final homogenization step in a ball mill with a rotation speed of 18 rpm and 25 mm balls for 24–48 h (depending on particle size) allows for the formation of homogeneous capillary suspensions without agglomerates. The solid content of the prepared capillary suspensions was between $\phi = 10$–20 vol%. Next to capillary suspensions consisting of one powder fraction, also mixtures consisting of glass 1 and glass 2 as well as glass 2 and glass 3 were used. Sintered parts with pore sizes in between those

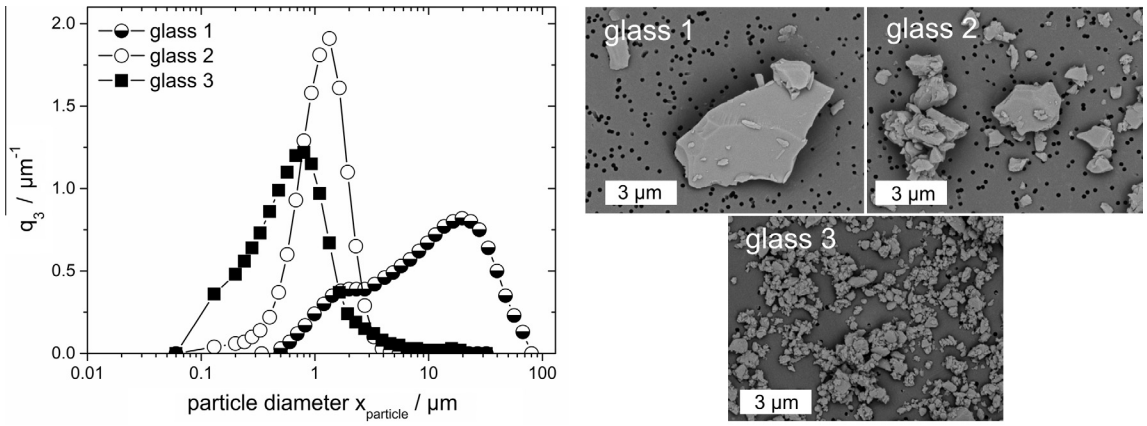

Fig. 1. Particle size analysis and SEM images of the used raw glass powders. Differential particle size distribution q_3 was determined through Fraunhofer diffraction.

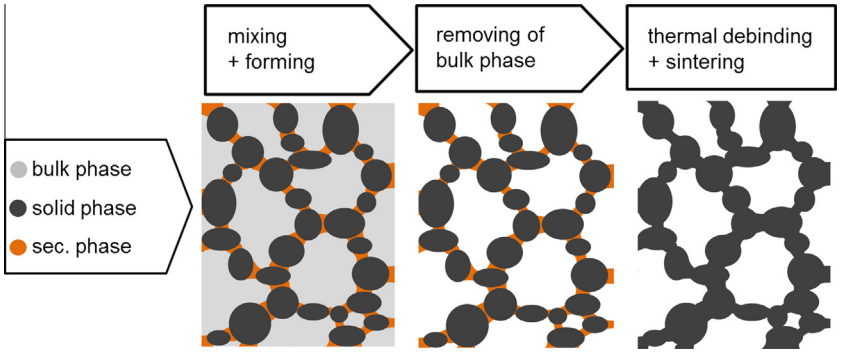

Fig. 2. Main steps of the processing route for manufacturing macroporous glass filters based on capillary suspensions.

obtained from suspensions including a single powder were thus available.

After the preparation of homogeneous, agglomerate-free capillary suspensions the pastes were molded by hand into sample forms and the top face was smoothed using a doctor blade. For mechanical strength tests we used rectangular forms with the size 50 mm × 12 mm × 5 mm and for filters we used circular forms with a diameter of 42 mm and a height of 5 mm. Placing the sample forms on an absorbing pad allowed debinding of the samples immediately after forming. Samples were bedded on an absorbing pad for 10 days at room temperature to debind the bulk phase by capillary extraction. The binder dissolved in the secondary phase crystallizes in the capillary bridges as the secondary phase is removed by evaporation and helps to create stable and portable green parts. The following thermal debinding step in a debinding oven at 200 °C (30 min) and 500 °C (60 min) on a porous ceramic plate ensured a complete and gentle debinding of the residual bulk fluid and the sucrose. The debinded samples were sintered at temperatures depending on the particle size of the solid powder such that an open porosity $\varepsilon = 50\%$ was reached for the sintered parts. Samples of glass 1 were sintered at 820 °C for 15 min, samples of glass 2 were sintered at 785 °C for 15 min and samples of glass 3 were sintered at 760 °C for 15 min. Sintering temperatures for the powder mixtures were in between the temperatures selected for the respective pure powders.

2.3. Characterization

Rheological characterization of the suspensions was done using a rotational rheometer (Haake Mars II; Thermo Scientific, Karlsruhe, Germany). A plate/plate geometry (diameter: 35 µm) was employed for viscosity measurements and a vane geometry (Z20 according to DIN 53019-1) for yield stress measurements [22]. Viscosity were obtained from shear rate ramp tests (shear rate range $\dot{\gamma} = 10$–1000 1/s), yield stress measurements were carried out using shear stress ramps (shear stress range $\sigma = 0.1$–1000 Pa). Yield stress values were calculated from deformation vs. stress curves according to the tangential method [23].

Surface and interfacial tension of the fluids were determined with a tensiometer (DCAT 11; DataPhysics Instruments GmbH, Filderstadt, Germany) equipped with a Wilhelmy-plate. For contact angle measurements we used an uncoated borosilicate glass cover slip (Carl Roth, Karlsruhe, Germany). The contact angles of the fluids to the used glass against air (θ_{Ba}, θ_{Sa}) were determined with the sessile-drop method (OCA 15; Dataphysics) by a numerical fit of the Young–Laplace equation to the imaged drop shape [24].

The porosity ε of the sintered parts was calculated from the Archimedes density according to DIN EN 993-1.

Image analysis of electron micrographs (Line Intercept Count Method [25]) was used to determine the pore size distribution of the sintered parts. Therefore, the sintered parts were infiltrated with epoxy resin and after grinding and polishing steps SEM cross-cut images (backscattering-mode, S-4500; Hitachi) were used for image analysis. Pore size distribution $q_3(x_{pore})$ and average pore size $x_{pore,av}$ were calculated from at least three SEM images. SEM imaging was chosen here for pore size characterization since it provides additional information about the pore shape in contrast to other methods like Hg-porosimetry.

For mechanical strength measurements the flexural strength σ_f (4-point bending test following DIN EN 843-1) and the compressive strength σ_c (following DIN 51104) were determined.

Permeability tests were performed to characterize filtration properties of the filter disks. The gas permeability was determined following DIN EN 993-4 and the liquid permeability (water as

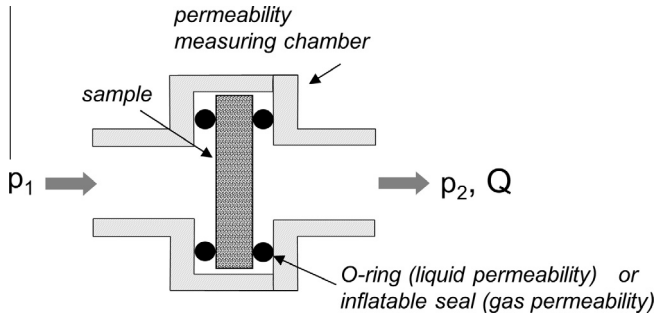

Fig. 3. Schematic model of equipment for gas and liquid permeametry.

liquid) was measured with a pressure strainer (DrM, Maennedorf, Switzerland). Volumetric flow rate was measured with a rotameter (for gas permeability) and an electronic balance (for liquid permeability), respectively. Gas and liquid permeability k_g and k_l of the porous glass disks was evaluated using Eq. (1):

$$k_{g/l} = \frac{L}{A}\eta\frac{Q}{\Delta p} \quad (1)$$

where $\Delta p = p_1 - p_2$ is the pressure drop between entrance and exit of the sample, k_g and k_l are Darcy's permeability coefficients, η the dynamic viscosity of the test fluid. L and A are the thickness and the cross sectional area of the sample, Q the volumetric flow rate of the fluid. Fig. 3 shows a schematic of the used measuring chamber. As-fired circular disks were grinded to an average diameter of 26 ± 1 mm and a height of 2 ± 0.1 mm for the filtration tests. We converted the gas flow Q at ambient pressure with the ideal gas law to the gas flow Q at the pressure predominant in the mid of the filter $p_M = (p_1 - p_2)/2$ to consider the compressibility. For each sample we chose up to 5 pairs of Δp and Q values to get a good average of the permeability k.

3. Results and discussion

With the extended Young-Dupré equation [21] the three-phase contact angle θ_{SB} of the material system was calculated from the surface tensions of the surrounding bulk phase Γ_{Ba} = 29.8 ± 0.2 mN/m and the secondary phase Γ_{Sa} = 76.1 ± 0.6 mN/m, the interfacial tension of the two fluids Γ_{SB} = 41.7 ± 0.2 mN/m and the contact angles of the fluids against air θ_{Sa} = 64.1 ± 3.2°, θ_{Ba} = 0°:

$$\cos\theta_{SB} = \frac{\Gamma_{Sa}\cos\theta_{Sa} - \Gamma_{Ba}\cos\theta_{Ba}}{\Gamma_{SB}} \quad (2)$$

The three-phase contact angle was calculated as θ_{SB} = 85.4 ± 5°, so the particles in this material system are connected via pendular shaped bridges [17].

3.1. Rheological characterization

Fig. 4 shows the yield stress σ_y and dynamic viscosity η for suspensions of glass particles with various secondary phase contents ϕ_{sec} up to 4 vol% of the total sample volume. At constant solids content ϕ and particle size $x_{50,3}$ we see a strong increase of yield stress and viscosity resulting from the structure formation in the capillary suspension. Increasing the secondary phase content to values ϕ_{sec} > 1 vol% results in a plateau of σ_y, since most of the capillary bridges are saturated. In this regime homogeneous capillary suspensions exist, which suit well as precursors for sintering materials [19,20].

Particle size also has a strong influence on the rheological behavior. Despite of the lower solids content in glass 2 suspensions ($x_{50,3}$ = 1.1 μm) compared to suspensions of glass 1 ($x_{50,3}$ = 11.0 μm), glass 2 suspensions have a higher yield stress. This results from the higher number of capillary bridges per volume in suspensions including smaller particles.

Our rheological data prove that we can create two fluid suspensions based on the glass particles used here. We get stable capillary suspensions with a characteristic structure formation similar to that already observed for other material systems [19–21] as will be discussed in the next section.

3.2. Structure formation: porosity and pore size

Porosity ε and average pore size $x_{pore,av}$ are the key parameters quantifying the structure of the sintered parts. In order to quantify the influence of the added secondary phase on structure formation constant sintering conditions (temperature profile, time) have been chosen for a given particle size.

SEM crosscut images of sintered parts consisting of glass 2 shown in Fig. 5 disclose the structural difference between sintered parts made from a regular and a capillary suspension. Both SEM images show a smooth pore shape but it is clearly visible that the pore structure changes drastically after addition of the secondary fluid. The open porosity ε increases from ~34% to ~50%, while the pore size increases nearly by a factor of 2, from $x_{pore,av}$ = 2.6 ± 0.2 μm to $x_{pore,av}$ = 4.0 ± 1.1 μm, comparing sintered parts from pure suspension to those from capillary suspensions. Similar behavior was found for suspensions of glass 1 and glass 3 and sintered parts made thereof, cf. Table 1. The strong increase

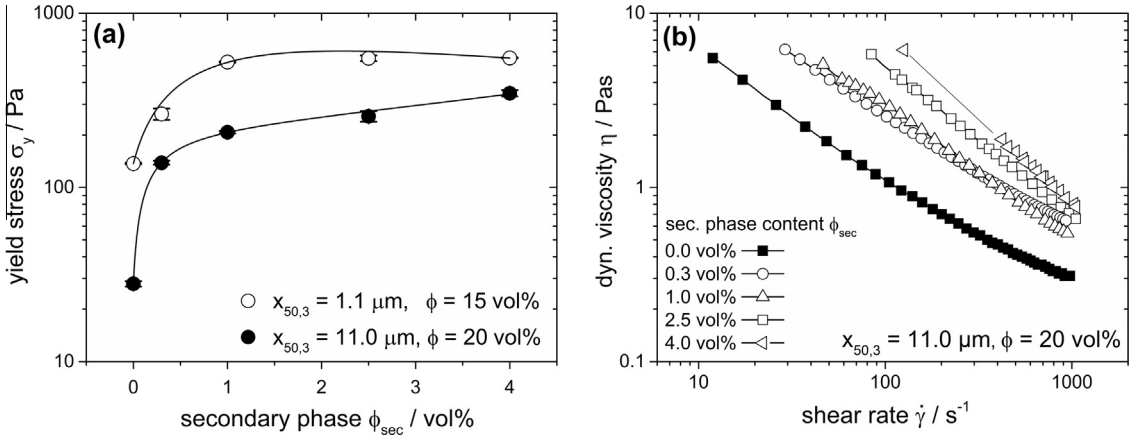

Fig. 4. (a) Yield stress σ_y vs secondary phase content ϕ_{sec} for capillary suspensions with two different average particle sizes $x_{50,3}$ and solids content ϕ, (b) dynamic viscosity η as a function of the shear rate for varying secondary phase content at constant solids content and constant particle size.

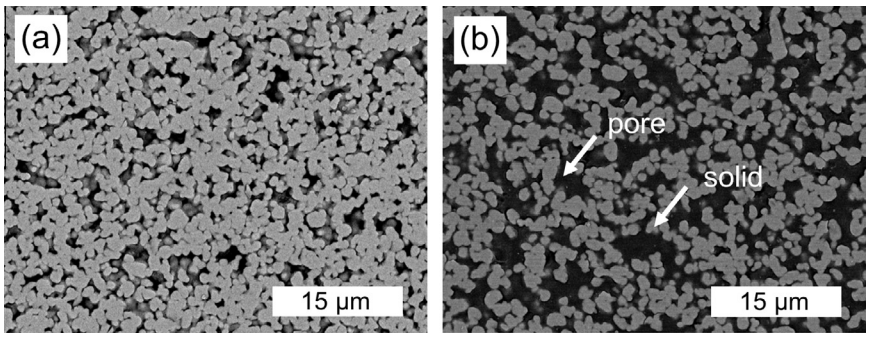

Fig. 5. SEM crosscut images of sintered parts of a pure suspension and a capillary suspension consisting of glass 2 as initial powder. (a) ϕ_{sec} = 0%, ε = 34%, $x_{pore,av}$ = 2.6 ± 0.2 µm, (b) ϕ_{sec} = 2.5%, ε = 51%, $x_{pore,av}$ = 4.0 ± 1.1 µm. Sintering conditions constant: T_{sinter} = 785 °C, t_{sinter} = 15 min. Solid particles appear light gray and pores as black.

Table 1
Yield stress data σ_y of suspensions and appropriate capillary suspensions, porosity ε and av. pore size $x_{pore,av}$ of sintered parts consisting of glass 1, glass 2 and glass 3 as initial powder. The given failures are the standard deviation of at least three measurements.

	Glass 1		Glass 2		Glass 3	
Sec. liquid ϕ_{sec} (vol%)	0.0	2.5	0.0	2.5	0.0	2.5
Yield stress σ_y (Pa)	28 ± 1	257 ± 18	137 ± 2	551 ± 21	139 ± 7	688 ± 72
Porosity ε (%)	18 ± 4	50 ± 1	34 ± 7	50 ± 2	39 ± 1	50 ± 2
Pore size $x_{pore,av}$ (µm)	–	49.6 ± 4.2	2.6 ± 0.2	4.0 ± 1.1	–	1.5 ± 0.1

of the yield stress in the wet state directly correlates to the increase in porosity and pore size in the solid state.

Changing the initial particle size allows for a variation of the average pore size in the sintered parts at constant porosity. This is shown in Fig. 6 displaying pore size distributions for sintered parts made from capillary suspensions based on the three glass powders shown in Fig. 1. Solids fraction in the wet suspensions and sintering conditions were adjusted that a constant porosity ε = 50% was achieved in all cases. The normalized differential pore size distributions q_3/q_3(modal) are mainly monomodal with a sharp cut to bigger pores. Obviously the pore size in the sintered part can be controlled directly by the initial particle size in the capillary suspension.

3.3. Mechanical strength

We determined the compressive and flexural strength of sintered parts made from capillary suspensions of the three different glass powders at a constant porosity ε = 50 ± 3%. Data shown in Fig. 7 are average values and standard deviations obtained from at least 10 specimen of each sample for compressive strength and 5 specimen of each sample for flexural strength. Average values of the compressive strength are between σ_c = 14.7–21.4 MPa and the flexural strength σ_f ranges between 4.6 and 10.3 MPa. Obviously, the average compressive strength is about a factor of two bigger than the flexural strength. As expected [20], the mechanical strength is essentially independent of the glass powder used and hence independent of the pore size of the sintered parts. Significantly lower values are found for the flexural strength of porous filters made from glass 3 and this is presumably due to inhomogeneities/cracks in the prepared specimen.

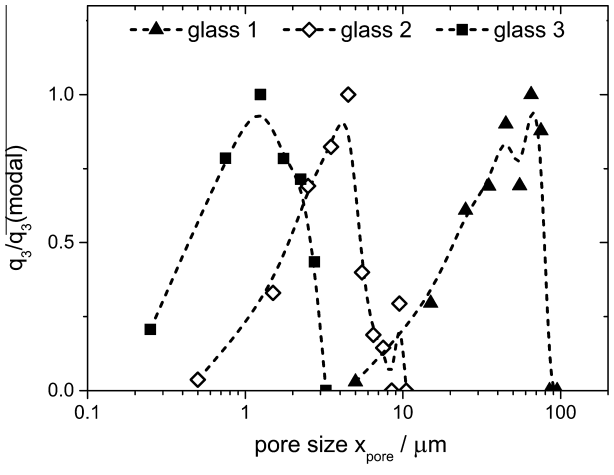

Fig. 6. Normalized differential pore size distribution q_3/q_3(modal) for sintered parts based on capillary suspensions, consisting of glass 1 (ϕ = 20 vol%, ϕ_{sec} = 2.5 vol%, T_{sinter} = 820 °C, t_{sinter} = 15 min), glass 2 (ϕ = 15 vol%, ϕ_{sec} = 2.5 vol%, T_{sinter} = 785 °C, t_{sinter} = 15 min) and glass 3 (ϕ = 20 vol%, ϕ_{sec} = 2.5 vol%, T_{sinter} = 760 °C, t_{sinter} = 15 min) as initial powder. Porosity ε = const. = 50 ± 3%. Pore size distributions determined via image analysis.

The mechanical strength of our porous glass samples is close to that of ceramic Al_2O_3 parts, manufactured via the same processing route and with similar porosity. It should be noted, that the mechanical strength of the dense ceramic matrix material is nearly an order of magnitude higher than that of glass. Dense α-Al_2O_3 has a compressive strength of about 4300 MPa and a flexural strength of 400 MPa [26], while the values of dense glass are only 800 MPa [27] and about 45–105 MPa (heavily dependent on surface quality). Flexural strength data for the used glass is provided from manufacturer (SCHOTT AG, Mainz, Germany).

SEM images of porous parts made from glass and ceramics are shown in Fig. 8. These images reveal a strong difference in pore circularity and pore roughness. While the glass sample shows smooth sinter necks with a high pore circularity, the ceramic Al_2O_3 sample has a rough and edged pore structure. This structure leads to a higher notch effect under load and results in a reduced mechanical strength. Thus despite the huge difference in the mechanical strength of the pure matrix material the corresponding values for the sintered porous parts from glass and ceramics are quite similar.

Gibson & Ashby [28] have developed a model describing the effect of open porosity on the mechanical strength and failure of cellular materials. The relative compressive strength of brittle porous materials, i.e. the compressive strength of the porous part σ_c normalized with the flexural strength of the dense material $\sigma_{f,0}$, is related to their open porosity ε as follows:

$$\frac{\sigma_c}{\sigma_{f,0}} = B_o(1-\varepsilon)^z \tag{3}$$

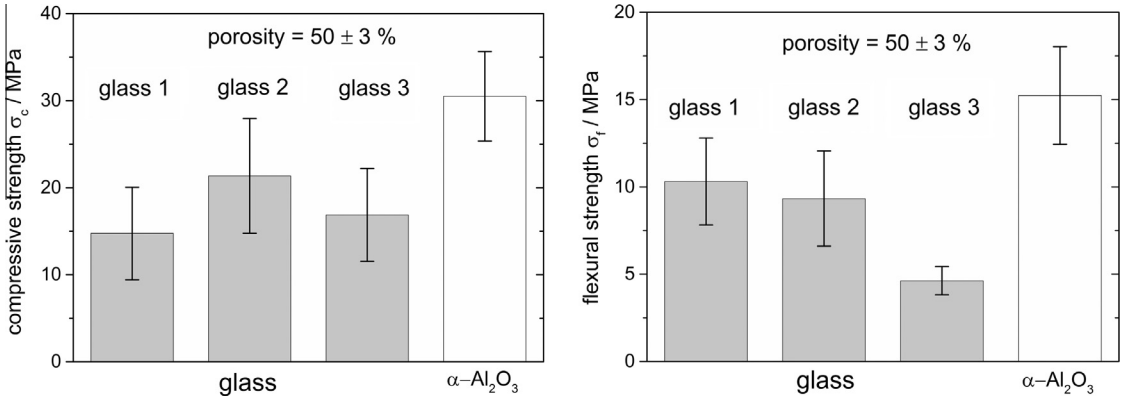

Fig. 7. Compressive strength σ_c and flexural strength σ_f of porous glass samples, compared with porous ceramic samples. All manufactured via capillary suspension processing.

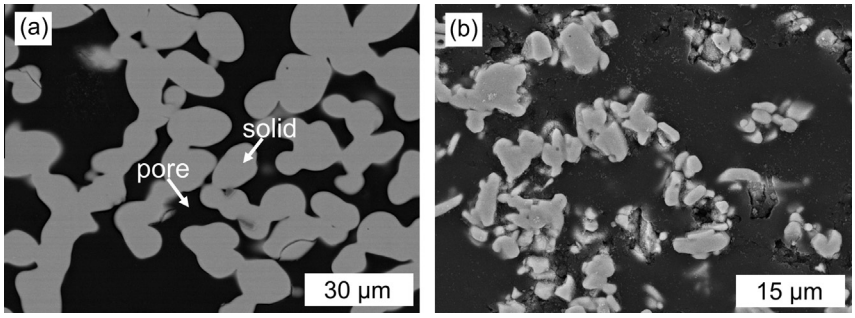

Fig. 8. SEM crosscut images of (a) a sintered glass sample (glass 1) and (b) a sintered ceramic sample, consisting of α-Al_2O_3. Solid particles appear light gray and pores as black.

The parameter z depends on the mode of failure. The exponent $z = 3/2$ was found to capture the behavior of brittle fracturing ceramic materials. B_0 is an empirical prefactor and the mechanical strength of a large variety of brittle cellular materials is described by Eq. (3) using $B_0 = 0.2$ [28]. Gauckler and coworkers [10] proved the Gibson & Ashby model to fit the experimental results for a large set of data on ceramic filters covering a wide porosity range selecting $B_0 = 0.2$ as prefactor in Eq. (3). Dittmann et al. showed that the mechanical strength of porous ceramic parts made from capillary suspensions is fairly well described by Eq. (3) with a prefactor $B_0 = 0.2$ but the dependence of mechanical strength on ε is somewhat stronger than derived by Gibson & Ashby [20].

Fig. 9 displays the relative compressive strength of glass and ceramic parts made from capillary suspensions for a broad range of relative density $1 - \varepsilon$. The relative compressive strength of the glass samples at a given porosity is significantly higher than that of the sintered ceramic parts. Fitting our glass data with the Gibson & Ashby model results in an empirical prefactor $B_0 = 0.8$ significantly higher than the value found for ceramic materials as mentioned above [10]. We attribute this improved strength to the rounder sinter necks in the glass samples which lead to a reduction of stress peaks in the porous material. Consequently the relative compressive strength increases drastically as already suggested based on SEM images shown in Fig. 8. Similar as previously reported by Dittmann et al. [20] we also find a slightly stronger dependence of relative compressive strength on porosity than suggested by Gibson & Ashby [28].

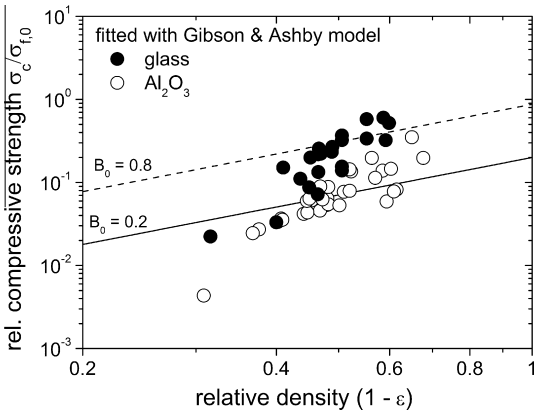

Fig. 9. Relative compressive strength of sintered samples of glass and α-Al_2O_3 as a function of the relative density $1 - \varepsilon$. The Gibson & Ashby model shows good agreement with the sintered capillary suspensions. Empirical prefactors: glass: $B_0 = 0.8$, Al_2O_3: $B_0 = 0.2$. Assumptions for the matrix flexural strength $\sigma_{f,0}$: Al_2O_3: 400 MPa, glass: 75 MPa [20].

3.4. Permeability

The permeability of a filter medium characterizes the mobility of a fluid in a porous structure. It is a function of the pore structure (porosity, pore size distribution, pore shape, tortuosity, etc.) and is generally independent of the test medium [29]. According to Darcy's law the permeability of a porous medium can be related to its porosity and pore size as follows [30,31]:

$$k_{g/l} = \varepsilon \frac{x_{\text{pore,av}}^2}{32T} \tag{4}$$

where $T > 1$ is the tortuosity factor describing the crookedness of a given pore structure; for straight cylindrical tubes $T = 1$. Fig. 10 shows the dependence of the liquid permeability k_l and the gas permeability k_g on the average pore size $x_{\text{pore,av}}$ of the tested filters from glass and Al_2O_3, at a constant open porosity

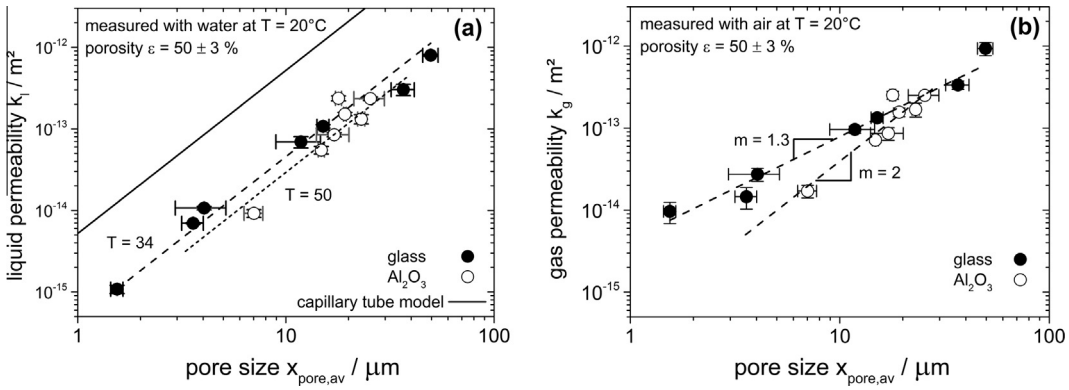

Fig. 10. (a) Liquid permeability k_l and (b) gas permeability k_g as a function of average pore size $x_{pore,av}$ of the filters. The solid line in (a) corresponds to the permeability of a filter consisting of straight circular tubes ($T = 1$) with the same porosity.

Table 2
Pore size data of commercial and capillary suspension product.

Product	Maximum pore size (µm) (acc. to manufacturer)	Average pore size $x_{pore,av}$ (µm) (from image analysis)
Commercial (DURAN, P5)	1.0–1.6	9.0 ± 0.3
Capillary suspension	–	1.5 ± 0.1

$\varepsilon = 50 \pm 3\%$. As expected, the permeability increases strongly with increasing pore size. Fitting Eq. (4) to the experimental liquid permeability data results in $T = 34$ for the filters made from glass capillary suspensions and $T = 50$ for the corresponding Al_2O_3 filters. Since the manufacturing process is the same for both types of filters we assume that the structure and its geometric tortuosity are similar but within the framework of this model the higher smoothness and circularity of the glass corresponds to a lower apparent tortuosity.

Liquid and gas permeability values are found to be similar for filters with pore diameter $x_{pore,av} > 10$ µm. For lower pore sizes liquid permeability is significantly lower than the gas permeability, at the lowest investigated pore size k_g is about an order of magnitude higher than k_l. For glass filters this effect is even more pronounced than for the ceramic filters and results in a weaker dependence of gas permeability on pore size than predicted by Darcy's law. Fig. 10b clearly confirms that gas permeability k_g for ceramic filters is well described by Eq. (4), whereas k_g scales with $x_{pore,av}^{1.3}$ for the glass filters. These differences between liquid and gas permeability might be attributed to the slip effect that can occur for gas flow through porous media with pore sizes on the length scale of the mean free path of the test gas. In particular at the necks between the pores additional Knudsen diffusion can get relevant and the so called Klinkenberg effect may occur finally leading to an increase of gas permeability k_g [29,32,33].

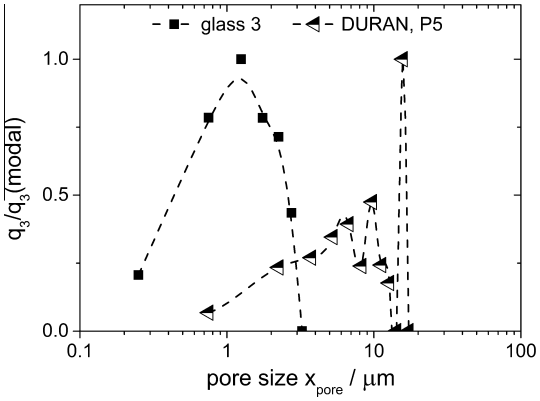

Fig. 12. Normalized differential pore size distribution q_3/q_3 (modal) for sintered parts based on capillary suspensions, consisting of glass 3 ($\varepsilon = \sim 50\%$) and the commercial product (DURAN P5, $\varepsilon = \sim 29\%$). Pore size distributions determined from image analysis.

Finally, for pore diameters $x_{pore,av} < 10$ µm the gas permeability is significantly higher for the glass filters than for the ceramic samples, e.g. for $x_{pore,av} = 4$ µm the extrapolated gas permeability value for Al_2O_3 filters is four times lower than for the corresponding glass samples, for the liquid permeability the filters of the two materials differ about a factor of two. The higher circularity and smoothness of the pores in the glass samples obviously is especially relevant at low average pore size.

3.5. Comparison with commercial products

We see strong differences comparing the microstructure, mechanical strength and permeability of capillary suspension based filters with readily available commercial filtration products,

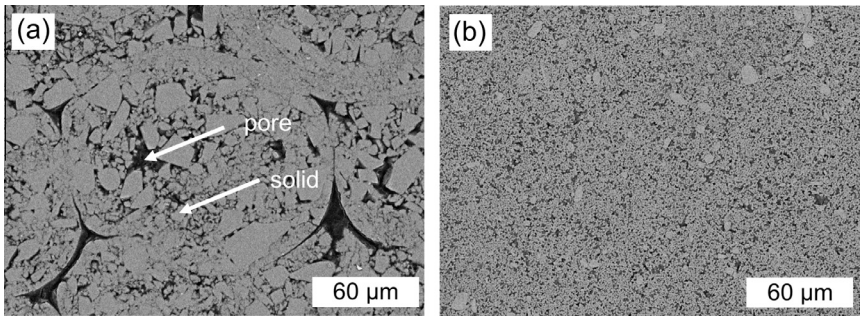

Fig. 11. SEM crosscut images of (a) commercial product (DURAN, P5): porosity $\varepsilon = \sim 29\%$, average pore size: $x_{pore,av} = 9.0 \pm 0.3$ µm; (b) capillary suspension product: $\varepsilon = \sim 50\%$, average pore size: $x_{pore,av} = 1.5 \pm 0.1$ µm. Solid particles appear light gray and pores as black.

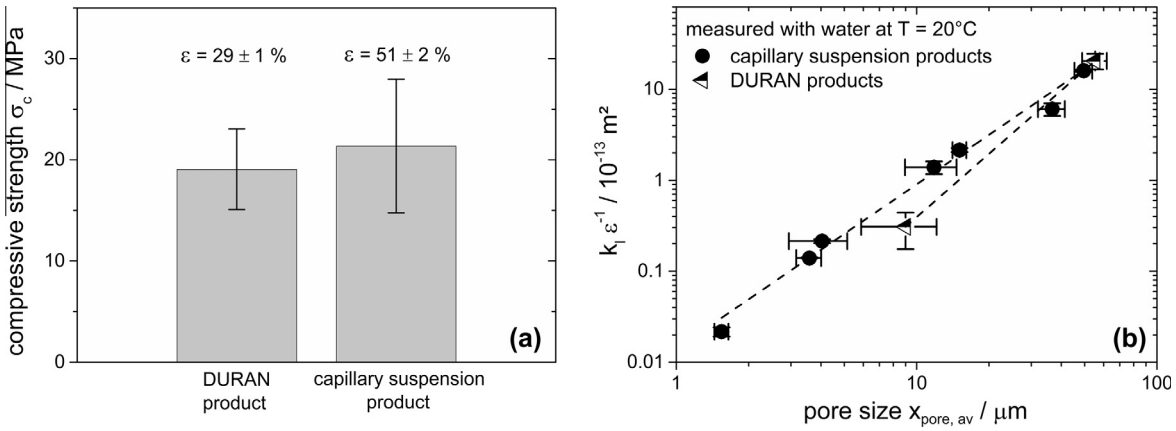

Fig. 13. (a) Comparison of compressive strength of a commercial product (DURAN) and a capillary suspension glass product. (b) Liquid permeability k_l normalized with porosity ε of capillary suspension glass products ($\varepsilon = 50 \pm 3\%$) compared with commercial products (DURAN) ($\varepsilon = 29 \pm 1\%$). Both consisting of glass.

both consisting of glass with nominal pore sizes in the same range (Table 2). Fig. 11 shows SEM crosscut images of the pore structure of two samples we will survey more intensively. The porosity of the commercial product DURAN P5 is $\varepsilon = 29 \pm 1\%$ whereas the corresponding value for the capillary suspension based product is almost twice as high ($\varepsilon = 50 \pm 2\%$). The commercial product shows an edged pore structure with strong inhomogeneities including some very large pores. In contrast the capillary suspension based product exhibits a very uniform pore structure. The inhomogeneous pore structure of the commercial product results in a broad pore size distribution (Fig. 12) and the average pore size is about 6 times higher than the nominal value provided by the manufacturer. The average pore size of the commercial product is $x_{pore,av} = 9.0 \pm 0.3$ µm, for the capillary suspension based product $x_{pore,av} = 1.5 \pm 0.1$ µm is found.

Fig. 13a shows the striking result that both samples exhibit essentially the same compressive strength despite of the much higher porosity of the capillary suspension based product. The large pores and sharp edges present in the commercial product are supposed to result in a strong notch effect and local stress peaks responsible for the failure of the commercial product.

We also investigated the liquid permeability of commercial and capillary suspension based products. Corresponding results for a series of capillary suspension based filters and two different commercial products are shown in Fig. 13b. Dividing liquid permeability k_l by the porosity ε accounts for the influence of the different product porosities. Especially the commercial product with $x_{pore,av} = 9.0 \pm 0.3$ µm exhibits a much lower reduced liquid permeability than corresponding capillary suspension based filters. This is particularly surprising since this material includes a fraction of very large pores (Fig. 11a) supposed to act as by-pass for the small pores (streaming pores). Presumably the higher circularity and smoothness of the pores as well as the high structural homogeneity of the capillary suspension based filters are decisive for their higher permeability.

4. Conclusions

The capillary suspension concept enables us to manufacture porous sintered glass filters with an open porosity of about 50% and average pore sizes $x_{pore,av}$ between 1 and 50 µm. The microstructure of the sintered glass parts is homogeneous with narrow, almost monomodal pore size distributions. Pores are much smoother and exhibit higher circularity than that of similarly processed ceramic filters.

The mechanical strength of the sintered glass parts is almost as high as that of Al_2O_3 parts with similar porosity, despite of the much lower strength of the dense matrix material. In other words the relative compressive strength $\sigma_c/\sigma_{f,0}$ of the glass parts is much higher than that of the ceramic filters. We trace this back to the differences in pore shape: The edged pore structure of the ceramic material leads to a higher notch effect and accordingly to a lower relative mechanical strength of the porous ceramic parts. Absolute values of the compressive strength agree well with the Gibson & Ashby model for brittle materials but the prefactor B_0 is higher for the glass filters than for porous ceramic materials. Moreover, the variation of the mechanical strength with porosity is slightly more pronounced than predicted by the exponent $z = 3/2$ theoretically deduced by Gibson and Ashby and experimentally confirmed for a broad variety of ceramic materials.

Glass filters based on capillary suspensions exhibit a higher gas and liquid permeability than corresponding ceramic filters. This is attributed to a higher pore smoothness and circularity in the glass parts. In accordance with Darcy's law liquid permeability varies as $x^2_{pore,av}$ for both types of filters, but apparent tortuosity is higher for the ceramic than for the glass filters. The high gas permeability found for the glass filters at low pores sizes is presumably due to slip in the necks between the pores with characteristic dimensions close to the mean free path of the gas and eventually results in a weaker dependence of k_g on pore size.

Finally, we compared glass filters manufactured according to our new processing route and commercial glass filters with respect to pore structure, mechanical strength and permeability. The commercial products have a broad pore size distribution with an inhomogeneous pore structure including a fraction of large holes and sharp edged pores. Although the capillary suspension based products exhibit porosities nearly twice as high as the commercial products, their mechanical strength is essentially equal. The high strength of capillary suspension based products is attributed to their uniform structure with smooth and highly circular pore shape contrasted by the investigated commercial product. This unique structural features are also decisive for the high permeability especially at low $x_{pore,av}$ found for the capillary suspension based filters.

Acknowledgements

This study was financially supported by the Bundesministerium für Wirtschaft und Energie (Project No. 03SHWB011) and Schott AG. Further thanks are given to Thomas Lebe for the work at the SEM-microscope as well as Daniel Müller and Monika Wolf for contributing to the permeability measurements.

References

[1] S. Ripperger, J. Altmann, Crossflow microfiltration – state of the art, Sep. Purif. Technol. 26 (2002) 19–31.
[2] The Freedonia Group, Membrane separation technologies – industry study with forecasts for 2016 & 2021, study #2872 (2012).
[3] O. San, C. Özgür, Fabrication of glassy ceramic membrane filters for filtration of spring water with clogging phenomena, J. Membr. Sci. 305 (2007) 169–175.
[4] C. Özgür, O. San, Fabrication of superhydrophilic membrane filters using spherical glass particles by ultrasonic spray pyrolysis, Ceram. Int. 37 (2011) 965–970.
[5] A. Lehtovaara, Ceramic-filter behavior in gasification, Bioresour. Technol. 46 (1993) 113–118.
[6] F.A. Acosta, A.H. Castillejos, J.M. Almanza, A. Flores, Analysis of liquid flow through ceramic porous media used for molten metal filtration, Metall. Mater. Trans. B 26B (1995) 159–171.
[7] B.K. Nandi, R. Uppaluri, M.K. Purkait, Identification of optimal membrane morphological parameters during microfiltration of mosambi juice using low cost ceramic membranes, Int. J. Food Sci. Technol. 44 (2011) 214–223.
[8] W. Yuan, Y. Tang, X. Yang, Z. Wan, Porous metal materials for polymer electrolyte membrane fuel cells – a review, Appl. Energy 94 (2012) 309–329.
[9] T.F. Zhao, C.Q. Chen, The shear properties and deformation mechanisms of porous metal fiber sintered sheets, Mech. Mater. 70 (2014) 33–40.
[10] A.R. Studart, U.T. Gonzenbach, E. Tervoort, L.J. Gauckler, Processing routes to macroporous ceramics: a review, J. Am. Ceram. Soc. 89 (2006) 1771–1789.
[11] J.C. Lee, H.J. You, H.S. Lee, M.C. Shin, J.S. Cha, S. Park, Pore formation in carbon-coated ceramic fiber filter media, Colloid. Surface. A 241 (2004) 185–190.
[12] D.B. Purchas, K. Sutherland, Handbook of Filter Media, second ed., Elsevier Advance Technology, Oxford, 2002.
[13] N. Lifshutz, On the 'mean flow' pore size distribution of microfiber and nanofiber webs, Int. Nonwovens J. 14 (2005) 18–24.
[14] A. Inayat, B. Reinhardt, H. Uhlig, W. Einicke, D. Enke, Silica monoliths with hierarchical porosity obtained from porous glasses, Chem. Soc. Rev. 42 (2013) 3753–3764.
[15] A. Santos, W. Vasconcelos, Properties of porous silica glasses prepared via sol–gel process, J. Non-Cryst. Solids 73 (2000) 145–149.
[16] K. Sutherland, Filters and Filtration Handbook, fourth ed., Elsevier Advance Technology, Oxford U.K, 2008.
[17] J. Reinhardt, J. Herwig, S. Rannabauer, M. Scheffler, D. Enke, Hierarchically structured glass monoliths based on polyurethane foams as template, J. Eur. Ceram. Soc. 34 (2014) 1465–1470.
[18] A. Sadighzadeh, M. Ghoranneviss, A. Salar Elahi, Application of partial sintering of waste glasses for preparation of porous glass bodies, J. Porous Mater. 21 (2014) 993–999.
[19] J. Dittmann, E. Koos, N. Willenbacher, Ceramic capillary suspensions: novel processing route for macroporous ceramic materials, J. Am. Ceram. Soc. 96 (2013) 391–397.
[20] J. Dittmann, N. Willenbacher, Micro structural investigations and mechanical properties of macro porous ceramic materials from capillary suspensions, J. Am. Ceram. Soc. 97 (2014) 3787–3792.
[21] E. Koos, N. Willenbacher, Capillary forces in suspension rheology, Science 331 (2011) 897–900.
[22] Q.D. Nguyen, D.V. Boger, Measuring the flow properties of yield stress fluids, Annu. Rev. Fluid Mech. 24 (1992) 47–88.
[23] R. Brummer, Rheology Essentials of Cosmetic and Food Emulsions, Springer-Verlag, Berlin Heidelberg, 2006.
[24] M. Bortolotti, M. Brugnara, C.D. Volpe, S. Siboni, Numerical models for the evaluation of the contact angle from axisymmetric drop profiles: a statistical comparison, J. Colloid Interface Sci. 336 (2009) 285–297.
[25] J. Russ, R. Dehoff, Practical Stereology, Kluwer Academic/Plenum Publishers, New York, 2000.
[26] E. Roos, K. Maile, Werkstoffkunde für Ingenieure: Grundlagen, Anwendung, Prüfung, fourth ed., Springer-Verlag, Berlin Heidelberg, 2011.
[27] G. Hauser, Hygienische Produktionstechnologie, Wiley-VCH Verlag, Weinheim, 2008.
[28] L. Gibson, M. Ashby, Cellular Solids: Structure and Properties, second ed., Cambridge University Press, Cambridge U.K., 1997.
[29] W. Tanikawa, T. Shimamoto, Klinkenberg effect for gas permeability and its comparison to water permeability for porous sedimentary rocks, Hydrol. Earth Syst. Sci. Discuss. 3 (2006) 1315–1338.
[30] F. Dullien, Porous Media: Fluid Transport and Pore Structure, second ed., Academic Press Inc., San Diego, 1992.
[31] F. Dullien, New network permeability model of porous media, AlChE J. 21 (1975) 299–307.
[32] J. Bear, Dynamics of Fluids in Porous Media, American Elsevier Publishing Company Inc, New York, 1972.
[33] M. Sahimi, Flow and Transport in Porous Media and Fractured Rock, second ed., Wiley-VCH, Weinheim, 2011.